View metadata, citation and similar papers at core.ac.uk
brought to you by CORE
provided by Aberdeen University Research Archive

Molecular-Level Insight into Selective Catalytic Reduction of NO_x with NH_3 to N_2 over Highly Efficient Bifunctional V_a-MnO_x Catalyst at Low Temperature

Ying Xin,[†] Hao Li,[†] Nana Zhang,[†] Qian Li,[†] Zhaoliang Zhang,[,†] Xiaoming Cao,*[,‡] P. Hu,[‡] Lirong Zheng,[§] and James A. Anderson*[,∥]*

[†]School of Chemistry and Chemical Engineering, Shandong Provincial Key Laboratory of Fluorine Chemistry and Chemical Materials, University of Jinan, Jinan 250022, China

[‡]Centre for Computational Chemistry and Research Institute of Industrial Catalysis, School of Chemistry and Molecular Engineering, East China University of Science and Technology, Shanghai 200237, China

[§]Institute of High Energy Physics, Chinese Academy of Sciences, Beijing 100049, China

[∥] Surface Chemistry and Catalysis Group, Materials and Chemical Engineering, University of Aberdeen, AB24 3UE, United Kingdom

ABSTRACT: Selective catalytic reduction of NO_x with ammonia (SCR) is not only an important model catalytic reaction, but also significant in terms of improving environmental air quality and human health. However, SCR catalysts suffer from the low activity and selectivity to N_2 at low temperature, which in part may be attributed to our limited understanding of the reaction mechanism. Here, an unambiguous molecular-level mechanism is presented for an improved low-temperature SCR activity using the bifunctional catalysts composed of highly active oxides (Mn_2O_3) for NH_3 activation and highly selective vanadates ($Mn_2V_2O_7$) which promote N_2 formation. NH_3 is initially activated by Mn_2O_3 to form an NH_2 intermediate. Transfer of NH_2 to $Mn_2V_2O_7$ then takes place which facilitates the capture of gaseous NO leading to the formation of NH_2NO over $Mn_2V_2O_7$, whereafter NH_2NO is efficiently converted to the preferred N_2 rather than the undesired by-product, N_2O. The proximity of the two components achieved *via* sol-gel preparation plays a crucial role in the transfer of active intermediates.

KEYWORDS: Nitrogen oxides; Selective catalytic reduction; Bifunctional catalyst; Density functional theory; Mechanism

1. INTRODUCTION

As one of the main fields of interest in environmental catalysis, nitrogen oxides (NO_x) removal using catalytic technologies has always received significant attention from researchers.[1] Selective catalytic reduction (SCR) of NO_x with ammonia (NH_3) is considered as the most efficient and widely used technology, however, developing the low-temperature active catalyst

(< 200ºC) with high N_2 selectivity still remains a challenge.[2,3] In general, the adsorption and activation of NH_3 on the acid sites of the catalysts is regarded as a key step in SCR reaction to enable NO_x conversion at low temperatures.[4,5] Furthermore, the activation of adsorbed NH_3 relies on an oxidizing component such as a transition metal oxide.[6-8] However, N_2 selectivity is exceptionally low while employing catalysts with adequate oxidation capability, such as Mn oxides (MnO_x).[2,3,9] MnO_x catalysts permit the high NO_x conversion at low temperature, while the selectivity to N_2 decreases due to the excessive activation of N-H bond and the resultant oxidation of NH_3 by NO, gaseous O_2 and bulk O.[3,10] Although the activity of MnO_x catalysts can be modified by changing the Mn oxidation state,[11] crystallinity,[3,12] as well as the surface area and morphology,[13] the low N_2 selectivity is still an inevitable drawback which must be overcome for the practical applications.[2,9,10]

In general, two plausible strategies have been adopted to enhance the low-temperature SCR performance of MnO_x catalysts.[2,9,10,14] One strategy is to synthesize bi- or multi-metal oxide catalysts to construct specific active sites which combine MnO_x with other metal oxides (Fe,[15] Ce,[16-18] Ni,[19] Nb,[20] Cr,[21] Zr,[22] etc.), or supported MnO_x on TiO_2,[23-26] SiO_2,[25,27] Al_2O_3,[25,28,29] zeolites[30-32], and carbon-based materials.[33-36] The improved activity and N_2 selectivity were thus achieved. The second approach is to prepare materials to develop the bifunctional catalysts, which involve the cooperation of two types of active sites with specific properties.[37-41] Several bifunctional catalysts that consist of an oxidation component (such as Mn, Mn-Ce, Mn-Cr, Mn-Cu, Mn/Ce-Zr oxides,[38,39,42] CoO_x-CuO_x/TiO_2,[43] etc.) and an SCR-active component (such as Fe-ZSM-5,[38,39] V_2O_5-WO_3/TiO_2,[39] Fe-beta,[42] $NiMn_2O_4$,[43] etc.) have received attention, in which V-based oxides possess high N_2 selectivity and resistance to sulfur oxide poisoning.[44,45] Specifically, vanadates attract intensive attention due to the higher thermal stability than V_2O_5.[46-

[50] However, vanadates have not been exploited to date as an active component of a bifunctional SCR catalyst.[46,47,49,51,52] Furthermore, the deceptively simple synergism between the oxidation component and the SCR-active component for the bifunctional catalysts still remains elusive at a molecular level.[53] For instance, Salazar et al. found that such a synergy completely vanished when the two components present as separate beds of an oxidation catalyst and an SCR catalyst. On this basis, they challenged the so-called "fast SCR" route and proposed a possible HNO_2 intermediate which may be formed over the oxidation component and proceeds to the SCR sites for further reaction. However, no spectroscopic or simulated/computed evidence was presented.[39]

In the present work, a Mn-V composite oxide (V_a-MnO_x) composed of NH_3 activation component (Mn_2O_3) and N_2 formation component ($Mn_2V_2O_7$) was prepared to probe the intrinsic SCR mechanism at low temperature from both an experimental and theoretical basis. Mn_2O_3 was confirmed to activate adsorbed NH_3 into a weakly adsorbed intermediate, NH_2, which can be transferred to $Mn_2V_2O_7$, where it reacts with the gaseous NO to form NH_2NO. The selective decomposition of NH_2NO into N_2 is far more favorable over $Mn_2V_2O_7$ than on Mn_2O_3. As a result, both the high activity and high N_2 selectivity are achieved over the bifunctional V_a-MnO_x catalyst at low temperature. This demonstrates a significant progress in balancing activity and selectivity of the two aspects of MnO_x-based SCR catalysts.

2. EXPERIMENTAL SECTION

Catalyst preparation. A series of V_a-MnO_x catalysts were prepared by a sol-gel method. A known amount of NH_4VO_3, $Mn(CH_3COO)_2$ and citric acid (CA) were mixed together in a

specific order with designated molar ratios. NH_4VO_3 was dissolved in 30 mL purified water at 70°C in a water bath under vigorous stirring, until the NH_4VO_3 had been fully dissolved and then held there for about 30 min. The corresponding quantity of CA was then slowly added to the solution and held for 30 min. The molar ratio of citric acid to the metal components (the total moles of vanadium and manganese) was fixed at 1.0. After that, the $Mn(CH_3COO)_2$ was added to the solution and stirred for 2 h. The suspension obtained was transferred to an evaporating dish and oven dried at 110°C overnight. The resulting materials were calcinated at 450°C for 5 h in muffle furnace in static air. The mixed oxides were denoted as V_a-MnO_x, where *a* represents the molar ratios of V/(V+Mn). Pure manganese oxide and vanadium-based oxide were synthesized using a similar procedure. For comparison and further investigation, oxidation phase (Mn_2O_3) and reactive phase ($Mn_2V_2O_7$) components were mechanically mixed with the $Mn_2V_2O_7$ to yield a materials consistent with $V_{0.05}$-MnO_x, and denoted as Mn_2O_3+$Mn_2V_2O_7$. Another reference sample denoted as MoO_3+$Mn_2V_2O_7$ was also synthesized by a similar procedure. Before SCR activity tests, the catalysts were pressed, crushed and sieved to 40-60 mesh.

Catalyst characterization. X-ray diffraction (XRD) patterns of the samples were recorded on a Bruker D8-FOCUS X-ray diffractometer using Cu Kα radiation (λ = 1.5418 Å) at 50 kV and 30 mA. Intensity data were collected over a 2θ range of 10-80° with a 0.03° step size and a counting time of 0.3 s per point. The relative amount of various components in V_a-MnO_x can be obtained using the quantitative XRD analysis by the reference intensity ratio (RIR) method.[54] Inductively coupled plasma-atomic emission spectrometer (ICP-AES) experiments were carried out on the IRIS Intrepid IIXSP instrument from Thermo elemental. Transmission electron microscopy (TEM) was conducted using a JEOL JEM-2010 microscope at an accelerating voltage of 200 kV. X-ray photoelectron spectroscopy (XPS) data were obtained on an Escalab

250Xi instrument from Thermo Fisher Scientific using monochromatic Al Kα radiation. To compensate for surface charging effects, the binding energies were calibrated using the C 1s hydrocarbon peak at 284.80 eV. X-ray absorption fine structure (XAFS) measurements at the Mn and V K-edges were performed in the transmission and fluorescence modes, respectively, at room temperature on the XAFS station of the 1W1B beam line of Beijing Synchrotron Radiation Facility (BSRF, Beijing, China), respectively. XAFS data were analyzed using the IFEFFIT software package.[55] Brunauer-Emmett-Teller (BET) surface areas were determined from N_2 adsorption/desorption isotherms using a Micromeritics ASAP2020M instrument. Before exposure to N_2, samples were outgassed at 300^{o}C for 5 h. Raman spectroscopy was obtained using a RM2000 (RENISHAW) with the 532 nm laser line. H_2-temperature programmed reduction (H_2-TPR) experiments were carried out on a TP-5000 Multifunctional Adsorption Instrument with a thermal conductivity detector (TCD) to monitor H_2 consumption. Before testing, 50 mg of sample was sieved to 40-60 mesh and pretreated at 400^{o}C for 30 minutes in a 30 mL/min flow of pure O_2, then cooled to room temperature in the same atmosphere. The reduction temperature was raised at 10^{o}C/min from 30 to 800^{o}C in a 30 mL/min flow of 5 vol.% H_2 in N_2. In order to quantify the total amount of H_2 consumed, a CuO standard was used for calibration purposes. NH_3-temperature programmed desorption (NH_3-TPD) experiments were performed in a quartz reactor using 50 mg of catalyst. NH_3 (m/z=16) was monitored using a quadrupole Mass Spectrometer (OmniStar 200, Balzers). Prior to experiment, the samples were pretreated at 400^{o}C for 30 min in 10 vol.% O_2/He (50 mL/min) and then cooled to 30^{o}C. NH_3 adsorption was performed in 4000 ppm NH_3 (50 mL/min) until the outlet NH_3 concentration remained constant. Samples were then purged with pure He for 1 h to remove weakly bound NH_3. Finally, the samples were heated to 500^{o}C at 10^{o}C/min. *In situ* infrared (IR) spectra were

recorded using a Bruker Tensor 27 spectrometer over the range 4000-400 cm^{-1}, with 16 scans, at a resolution of 4 cm^{-1}. Self-supporting wafers were pretreated in the cell at 400°C in a flow of He for 30 min to remove any adsorbed species. After cooling to ambient temperature, a background spectrum was recorded. The IR spectra were recorded at room temperature in a flow of 500 ppm NH_3+He balance or 500 ppm NH_3+500 ppm NO+5.3 vol.% O_2+He balance (150 mL/min). The samples were then heated to 250°C at 10°C/min.

Catalytic activity. The steady state SCR activity over V_a-MnO_x catalysts and the reference samples were tested in a fixed-bed quartz tube reactor (6.0 mm i.d.) with a thermocouple placed inside the catalyst bed in the temperature range 150-450°C. In SCR reactions, the model flue gas consisted of 500 ppm NO, 500 ppm NH_3, 5.3 vol.% O_2 and He balance. The total flow rate was maintained at 300 mL/min corresponding to a gas hourly space velocity (GHSV) of 50 000 h^{-1}. Concentrations of NO and NO_2 were monitored by a chemiluminiscence NO_x analyzer (42*i*-HL, Thermo). N_2O and NH_3 were determined by quadrupole mass spectrometer (MS, OmniStar 200, Balzers) using the m/z of 44 for N_2O, and 17 for NH_3. The data for steady-state activity of catalysts were collected after about 1 h on stream. From the concentration of the gases at steady state, the NO_x conversion and N_2 selectivity were calculated according to the following equations:

$$NO_x \text{ conversion } (\%) = \frac{[NO_x]_{in} - [NO_x]_{out}}{[NO_x]_{in}} \times 100\%$$

$$N_2 \text{ selectivity } (\%) = \frac{[NO_x]_{in} + [NH_3]_{in} - [NO_x]_{out} - [NH_3]_{out} - 2[N_2O]}{[NO_x]_{in} + [NH_3]_{in} - [NO_x]_{out} - [NH_3]_{out}} \times 100\%$$

By assuming conditions free from diffusion limitations were met, the SCR reaction rates normalized by sample mass and BET surface area of the catalyst can be calculated according to the following equation:[4]

$$\text{Rate}=\frac{X_{\text{NO}}QC_{\text{f}}}{V_{\text{m}}W(S_{\text{BET}})}$$

where X_{NO} is the NO conversion at a steady SCR reaction temperature (100 ^{o}C) (%), Q is the volumetric flow rate (300 mL/min) and C_f is the feeding concentration of NO (500 ppm). V_m is the molar volume of gas (22.4 mL/mol), W is the sample weight (g) and S_{BET} is the BET surface area of the catalyst (m^2/g).

3. THEORETICAL CALCULATIONS

To understand the relevant structural and electronic properties of Mn_2O_3 and $Mn_2V_2O_7$ materials and the SCR network occurring on their surfaces at a molecular level, the spin polarized first-principles calculations based on density functional theory (DFT) implemented in the Vienna *ab initio* Software Package (VASP)[56,57] were performed with a plane-wave kinetic energy cutoff of 500 eV. The projector augmented wave (PAW) pseudo potentials[58] were utilized to describe the valence-core interactions. The exchange-correlated term was described utilizing generalized gradient approximation (GGA) of Perdew-Burke-Ernzerhoff (PBE).[59] The PBE+*U* approach was also used to address the on-site Coulomb interactions in the localized d orbitals of Mn and V cations through an additional Hubbard-type *U* term.

For Mn_2O_3, since it will be converted from orthorhombic structure (space group *Pcab*) to cubic structure (space group *Ia3*) in the form of α phase once the temperature is above 308 K[60]

which is lower than the SCR reaction temperature, a cubic conventional unit cell of α-Mn_2O_3 containing 16 units of Mn_2O_3 with the equilibrium lattice constant of 9.658 Å was investigated. The effective U = 4.0 eV fitted according to its oxidation energy[61] was utilized for the Mn cation at α-Mn_2O_3. The exposed Mn_2O_3(202) surface found by TEM was modeled by a 4-layer p(1×1) slab of 8.364 Å × 8.364 Å separated by a ~10 Å vacuum in Z direction utilizing 4 × 4 × 1 k-point mesh for Brillouin integration.

$Mn_2V_2O_7$ exists in the form of β-$Mn_2V_2O_7$ with a thortveitite-like structure in a monoclinic system of space group *C2/m* at the reaction temperature.[62] Hence, the bulk β-$Mn_2V_2O_7$ containing 2 $Mn_2V_2O_7$ units within a unit cell of 6.710 Å × 8.726 Å ×4.970 Å was modeled as the most stable ferromagnetic (FM) states.[63] The effective U = 4.0 and 3.1 eV as reported for isovalent binary metal oxides[61] were utilized for Mn and V, respectively. For the exposed $Mn_2V_2O_7(\bar{2}01)$ surface, there are two possible terminations. The only difference between $Mn_2V_2O_7(\bar{2}01)$-A and $Mn_2V_2O_7(\bar{2}01)$-B terminals is the existence of the exposed one-fold coordinated oxygen anion (O_{1c}). The more stable $Mn_2V_2O_7(\bar{2}01)$-A terminal with O_{1c} was studied during this reaction. We refer to $Mn_2V_2O_7(\bar{2}01)$-A as $Mn_2V_2O_7(\bar{2}01)$ hereinafter. The stoichiometric exposed β-$Mn_2V_2O_7(\bar{2}01)$ surface was modeled by a 6-layer p(1×1) slab of 6.868 Å ×6.868 Å separated by a ~10 Å vacuum in Z direction utilizing 4 × 4 × 1 k-point mesh for Brillouin integration.

For both Mn_2O_3(202) and $Mn_2V_2O_7(\bar{2}01)$ surfaces, during the geometry optimization, the bottom two layers were fixed while the adsorbates and the other layers were relaxed until the force of each atom was lower than 0.05 eV/Å. The transition states (TSs) were determined within a constrained minimization scheme with the same force convergence criterion.[64-66] Each TS was further verified as the first-order saddle with only one imaginary vibrational frequency and the

corresponding vibrational mode along the reaction coordination based on the numerical vibrational frequency analysis.

The adsorption energies of reactants were calculated following:

$$E_{ad}(x) = E(slab) + E(x) - E(x/\text{slab})$$

where $E(slab)$, $E(x)$ and $E(x/\text{slab})$ are the total energies of the catalyst surface, x in the gas phase and x adsorbed on the catalyst surface, respectively. The more positive $E_{ad}(x)$ is, the more strongly the species x binds with the surface. The adsorption energies were also checked utilizing the screened hybrid functional of Heyd-Scuseria-Ernzerhoff functional (HSE06)[67] at the optimized structure obtained from PBE+U level.

4. RESULTS AND DISCUSSION

4.1 Structural characterization and catalytic activity

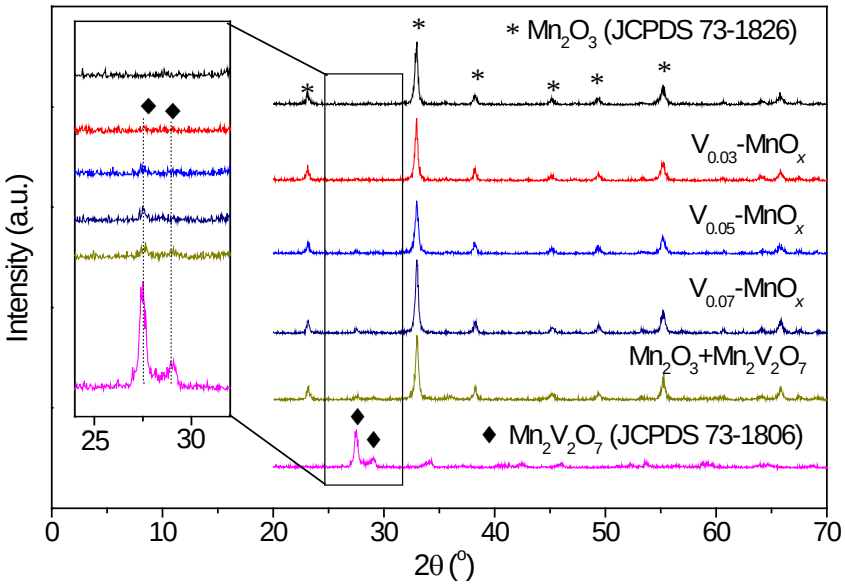

Figure 1. XRD patterns of V_a-MnO_x, Mn_2O_3, $Mn_2V_2O_7$ and reference samples.

Table 1. ICP, XRD, XPS, surface areas, H_2-TPR, and NH_3 desorption data for V_a-MnO_x.

Samples	ICP data		Theoretical values		XRD		XPS			Surface area (m^2/g)	H_2-uptake (μmol/g)	NH_3 desorption		
	V (wt.%)	Mn (wt.%)	V/Mn molar ratio	V/Mn molar ratio	$Mn_2V_2O_7$ (wt.%)	$Mn_2V_2O_7$ (wt.%)	Mn_2O_3/ $Mn_2V_2O_7$ molar ratio	Surface V/Mn molar ratio	$O_\alpha/(O_\alpha+O_\beta)$ (%)			(μmol/g)	(μmol/m^2)	Theoretical (μmol/m^2)
Mn_2O_3	--	68.59	--	--	0	0	0	0	35.7	31.9	1128	27.01	0.85	0.85
$V_{0.03}$-MnO_x	1.53	65.49	0.03	0.03	6.0	4.7	32.1	0.03	33.9	28.9	1209	37.32	1.29	0.93
$V_{0.05}$-MnO_x	2.64	63.90	0.04	0.05	10.2	10.4	18.1	0.05	34.7	39.2	1239	47.72	1.22	1.00
$V_{0.07}$-MnO_x	3.77	64.75	0.06	0.07	14.3	14.2	12.3	0.05	32.5	32.3	1062	40.61	1.26	1.06
$Mn_2V_2O_7$	33.67	34.95	1.03	1	100	100	--	0.69	22.2	15.5	1125	35.62	2.29	2.29
Mn_2O_3+ $Mn_2V_2O_7$	3.06	67.36	0.05	0.05	10.2	10.0	18.5	0.67	24.3	31.1	1332	--	--	--

XRD patterns show that V_a-MnO_x composite oxides contain Mn_2O_3 (JCPDS No. 73-1826, orthorhombic) and $Mn_2V_2O_7$ (JCPSD No. 73-1806, monoclinic) phases (Figure 1). The contents of $Mn_2V_2O_7$ from the quantitative XRD analysis coincide with the theoretical values and ICP data, indicating that the doped V might exist in the form of $Mn_2V_2O_7$ (Table 1). On the basis of the similar Mn K-edge X-ray absorption near edge structure (XANES) spectra and radial structure function (RSF) curves for Mn_2O_3 and V_a-MnO_x (Figure S1), most of the Mn atoms in V_a-MnO_x are trivalent and in octahedral coordination, and others are in the form of $Mn_2V_2O_7$ according to XRD (Figure 1). On the other hand, two peaks are recognized at ~1.7 Å and ~3.1 Å

in the RSF curves of $Mn_2V_2O_7$, corresponding to the Mn^{2+}-O and Mn^{2+}-V shells, respectively. In the case of the V K-edge, the peak position and shape of the normalized XANES and RSF (Figure 2) curves for V_a-MnO_x correspond well with those of $Mn_2V_2O_7$ and Mn_2O_3+$Mn_2V_2O_7$, consistent with the XRD patterns (Figure 1 and Table 1) confirming that all of the V atoms in V_a-MnO_x exist in the same tetrahedral coordination environment as in $Mn_2V_2O_7$.[68] Raman spectra also show the $Mn_2V_2O_7$ phase for $V_{0.07}$-MnO_x (Figure S2).

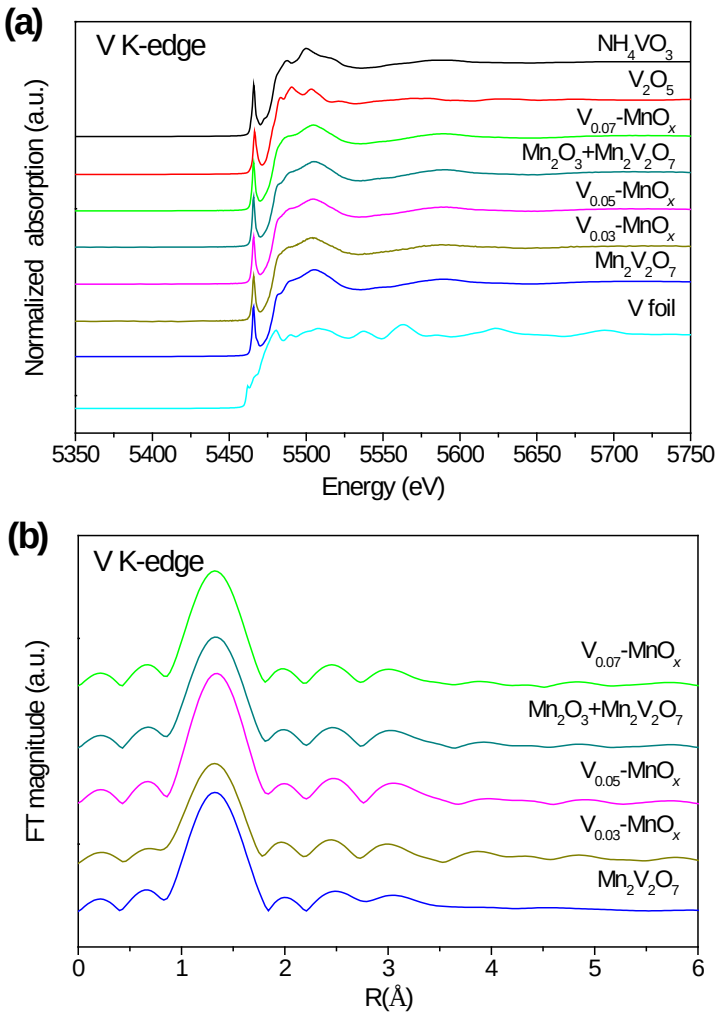

Figure 2. Normalized XANES spectra (a) and the RSF curves (b) of V K-edge for V_a-MnO_x and the reference samples.

XPS was further used to characterize the surfaces of V_a-MnO_x. For Mn_2O_3 and V_a-MnO_x, no obvious change in binding energies of Mn 2p was observed due to the excess Mn_2O_3 in V_a-MnO_x (Figure S3a). As for $Mn_2V_2O_7$, the Mn $2p_{3/2}$ binding energy was located at 640.8 eV, which is attributed to Mn^{2+}.[7] Compared with those of $Mn_2V_2O_7$ and Mn_2O_3+$Mn_2V_2O_7$, the binding energies of V 2p for V_a-MnO_x show an obvious shift toward lower values, indicating a reduction in the oxidation state of V,[69,70] probably due to the the strong interaction between Mn_2O_3 and $Mn_2V_2O_7$ (Figure S3b). The O 1s peaks can be fitted using two oxygen species, the lattice oxygen at ~529.9 eV (O_β) and the chemisorbed surface oxygen at ~531.1 eV (O_α) (Figure S3c).[7] The close values of [O_α/(O_α+O_β)] for V_a-MnO_x to Mn_2O_3, which are much higher than those in $Mn_2V_2O_7$ and Mn_2O_3+$Mn_2V_2O_7$, guarantee the activition of NH_3 on V_a-MnO_x. The approximate V/Mn atomic ratio of V_a-MnO_x to ICP and theoretical values also suggest that V is not enriched on the surface.

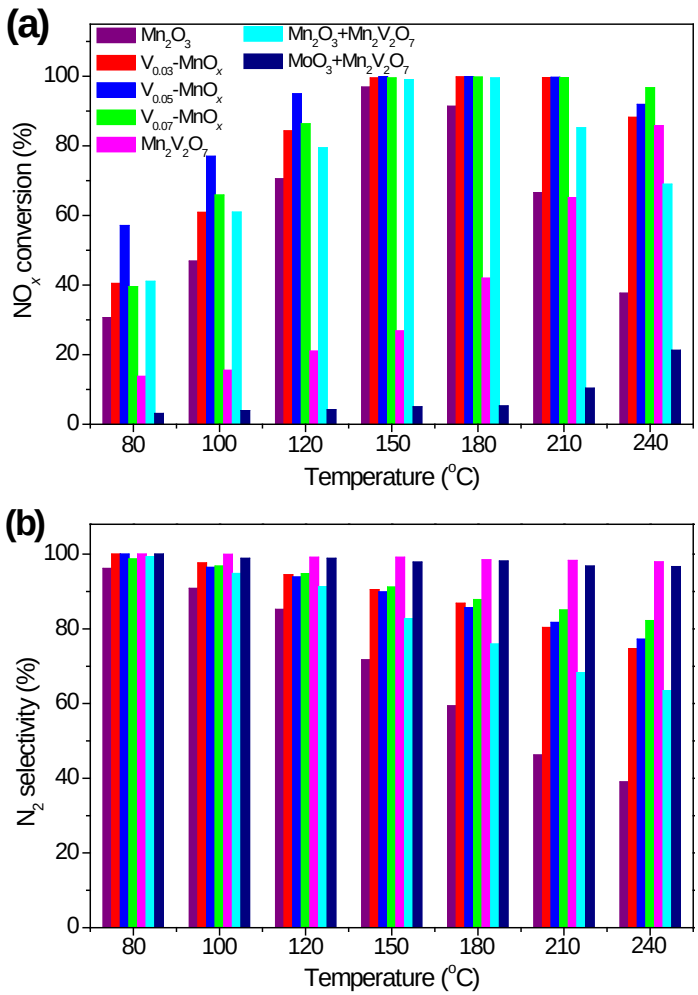

Figure 3. (a) NO_x conversion and (b) N_2 selectivity for V_a-MnO_x, Mn_2O_3, $Mn_2V_2O_7$ and reference samples.

NO conversion and selectivity to N_2 are shown in Figure 3. Mn_2O_3 is active in SCR reaction over the whole temperature range, however, N_2 selectivity decreases significantly with increasing temperature. In contrast, $Mn_2V_2O_7$ exhibits much lower activity with excellent N_2 selectivity. Evidently, both NO_x conversion and N_2 selectivity were improved for V_a-MnO_x. In particular, $V_{0.05}$-MnO_x shows NO_x conversions above 90% between 120 and 240°C, and the N_2 selectivity was always above 80%. Furthermore, NO_x conversion to N_2 for $V_{0.05}$-MnO_x is higher

than that of the Mn_2O_3+$Mn_2V_2O_7$ sample, which constitutes the arithmetic sum of individual components with the same component content as $V_{0.05}$-MnO_x, at measured temperatures, suggesting the existence of synergism between Mn_2O_3 and $Mn_2V_2O_7$ in $V_{0.05}$-MnO_x. However, if Mn_2O_3 is replaced by an equivalent non-oxidant MoO_3, NO_x conversion is even lower than that of $Mn_2V_2O_7$, confirming that the presence of Mn_2O_3 is indispensable for the reaction. Moreover, the samples did not undergo structural modifications during the SCR reactions (Figure S4).

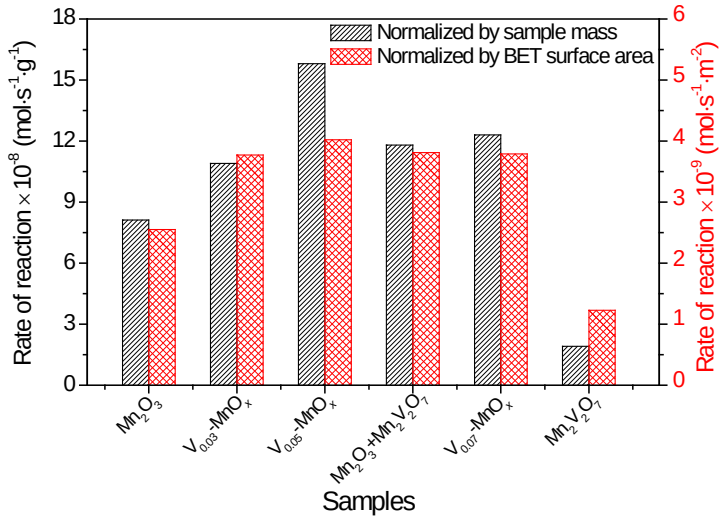

Figure 4. Reaction rates at 100°C for V_a-MnO_x, Mn_2O_3, $Mn_2V_2O_7$ and reference samples.

Figure 4 shows the reaction rates for NO_x conversion to N_2 in the kinetic regime at 100°C. The activity for N_2 production is improved over V_a-MnO_x on the basis of the specific rate per gram and per surface area, and $V_{0.05}$-MnO_x is the most active for N_2 production. Furthermore, the Mn_2O_3+$Mn_2V_2O_7$ sample shows similar behavioral trends but to a less extent than $V_{0.05}$-MnO_x.

This again indicates that the improved activity of V_a-MnO_x has a basis in the synergism between Mn_2O_3 and $Mn_2V_2O_7$.

4.2 Redox and acid properties

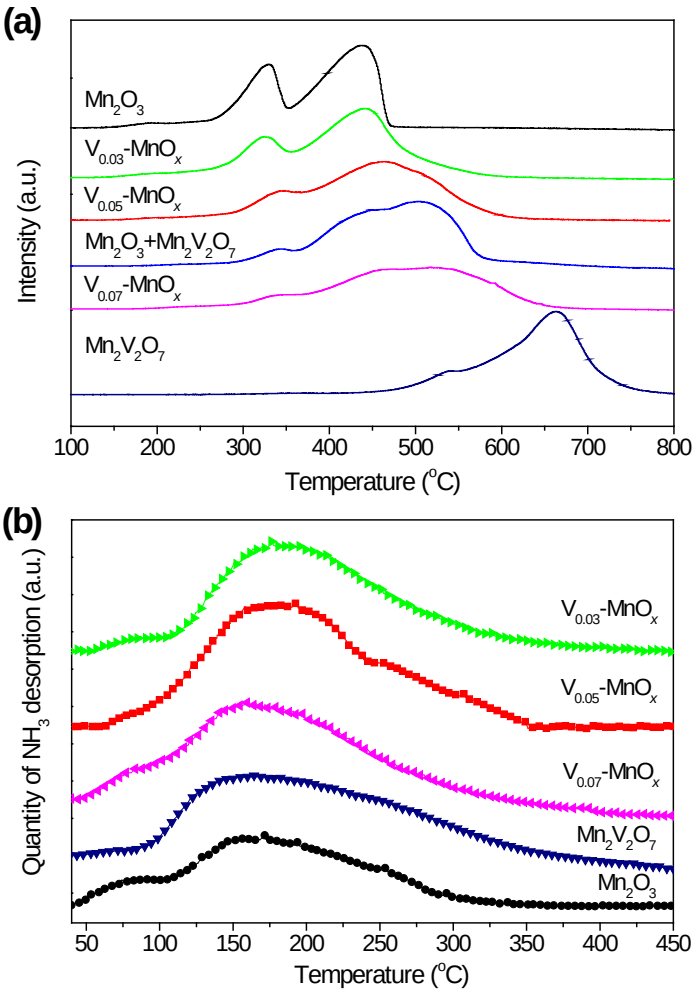

Figure 5. (a) H_2-TPR profiles for Mn_2O_3, $Mn_2V_2O_7$, V_a-MnO_x and reference samples, and (b) NH_3-TPD profiles of Mn_2O_3, $Mn_2V_2O_7$, and V_a-MnO_x.

Mn-based catalysts have been reported to show the improved SCR activity due to their strong redox properties.[10] Hence, H_2-TPR patterns of V_a-MnO_x (and references) were performed (Figure 5a). Based on the XRD patterns of the samples after SCR reactions (Figure S5), the reduction products of Mn_2O_3 and $Mn_2V_2O_7$ are MnO and MnV_2O_4, respectively. Mn_2O_3 shows peaks at 328 and 440°C, which are assigned to the reduction of Mn_2O_3 to Mn_3O_4 and Mn_3O_4 to MnO, respectively. $Mn_2V_2O_7$ shows only a high-temperature reduction peak above 500°C, corresponding to the transformation, V^{5+} ($Mn_2V_2O_7$) to V^{3+} (MnV_2O_4). The low-temperature redox peaks of V_a-MnO_x could be attributed to the reduction of Mn species. However, compared with pure Mn_2O_3 and $Mn_2V_2O_7$, the Mn^{3+} reduction to Mn^{2+} is shifted to higher temperature while the reduction of V^{5+} into V^{3+} starts at a lower temperature in V_a-MnO_x, suggesting synergistic effects between Mn_2O_3 and $Mn_2V_2O_7$ in V_a-MnO_x possibly involving H spillover from Mn_2O_3 to $Mn_2V_2O_7$, which results in the simultaneously suppression of Mn^{3+} reduction and promotion of the V^{5+} reduction. In addition, the primarily quantitive H_2 consumption is very close (Table 1).

Acidity is another crucial factor in SCR reactions.[71] To determine this aspect of these samples, NH_3-TPD was carried out (Figure 5b) and the corresponding desorption quantities were calculated (Table 1). More NH_3 was desorbed from V_a-MnO_x compared with Mn_2O_3, $Mn_2V_2O_7$, and the theoretical mass-weighted arithmetic values calculated from the corresponding weight ratio of Mn_2O_3 and $Mn_2V_2O_7$ in V_a-MnO_x, which would be consistent with synergistic effects arising between Mn_2O_3 and $Mn_2V_2O_7$ for the V_a-MnO_x samples. In addition, the temperature range of NH_3 desorption is consistent with the active temperature window for SCR of V_a-MnO_x. The maximum NH_3 desorption per gram sample was obtained for $V_{0.05}$-MnO_x which also shows the highest reaction rate (Table 1 and Figure 4). However, the NH_3 desorption amount per unit

surface area of V_a-MnO_x was nearly identical (Table 1), suggesting that the promoted SCR performance of V_a-MnO_x originate from the increased acid amounts in despite of their various compositions.

4.3 *In situ* IR spectra of NH_3 adsorption

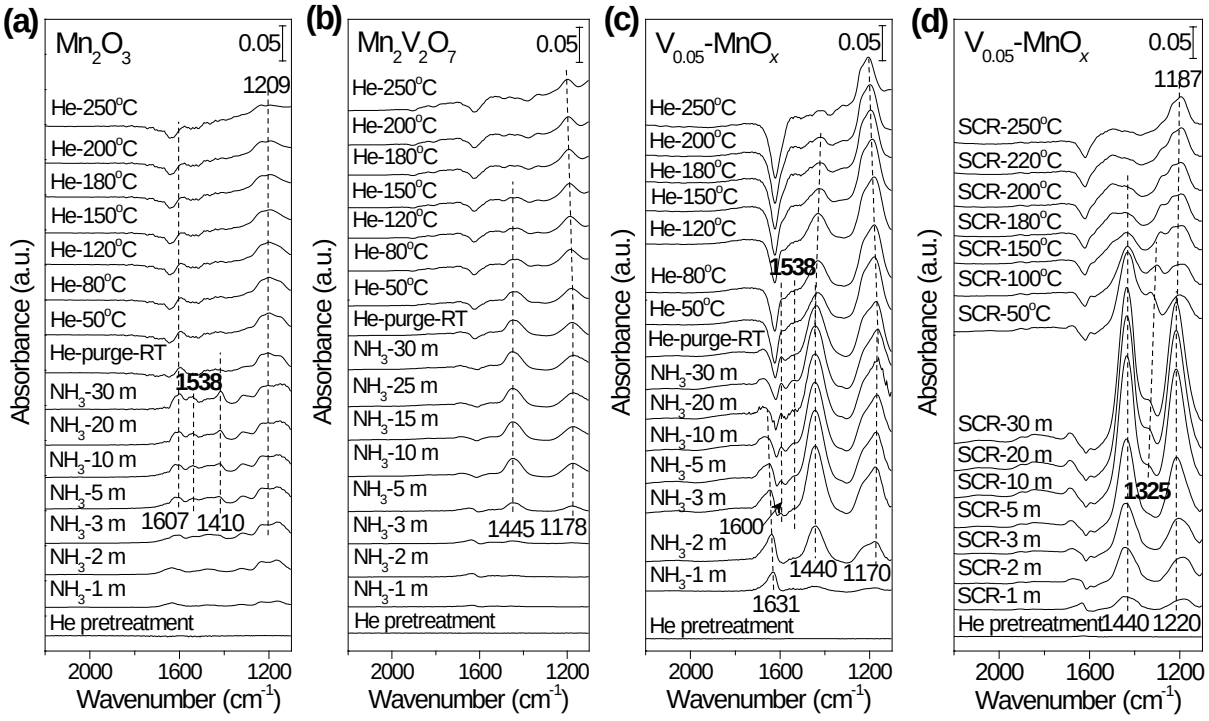

Figure 6. *In situ* IR spectra of (a-c), NH_3 adsorption at steady-state and (d) during SCR reaction over (a) Mn_2O_3, (b) $Mn_2V_2O_7$ and (c, d) $V_{0.05}$-MnO_x.

To investigate the nature of the adsorbed NH_3 species and potential reaction intermediates, *in situ* IR spectra were collected of NH_3 adsorption at room temperature and subsequent desorption with increasing temperature (Figure 6a-c). Only ammonia adsorption at Lewis acid sites was

observed for Mn_2O_3 (Figure 6a), which is supported by the absence of negative bands about 3600 cm^{-1} (Figure S6a).[45,71-73] Bands at ~1209 and ~1607 cm^{-1} are attributed to the symmetric and asymmetric bending modes of NH_3 coordinately linked to Lewis acid sites, respectively.[72] The weak band at 1410 cm^{-1} disappears completely after He purging at room temperature, which is derived from the protonation of weakly adsorbed NH_3.[29] Notably, a band at 1538 cm^{-1} was observed for Mn_2O_3, which is attributed to the scissoring vibration mode of weakly adsorbed NH_2 (amide) species arising from the partial oxidation of NH_3 (H-abstraction),[74] because it disappears after the He purge at room temperature.[72]

In addition, for $Mn_2V_2O_7$, evidence for both Brønsted and Lewis acid sites was observed from Figure 6b, while the IR spectra of $V_{0.05}$-MnO_x exhibits the combined characteristics of Mn_2O_3 and $Mn_2V_2O_7$ (Figure S6b and 6c). The bands at 3353-3028 cm^{-1} arise from N-H stretching vibrations of NH_3 adsorbed on Lewis sites (Figure S6b). The corresponding bending vibrations are observed at 1170/1178 cm^{-1}(Figure 6c).[75-77] The characteristic bands for NH_4^+ formed by the interaction of NH_3 with Brønsted sites around 1440 cm^{-1} (Figure 6c) are also supported by the negative band at 3660-3670 cm^{-1} (Figure S6b), which indicates the consumption of the -OH. The enhanced quantities of Lewis and Brønsted acidity in $V_{0.05}$-MnO_x compared with those of Mn_2O_3 and $Mn_2V_2O_7$ are again potentially indicative of synergistic effects between the components, in accordance with the NH_3-TPD results (Figure 5b and Table 1). In addition, NH_3 bound to Lewis acid sites were more strongly adsorbed,[72] because the intensity of bands due to Brønsted acid sites decreased noticeably with the increasing temperature, while those due to adsorption at Lewis acid sites still remained. Importantly, the NH_2 species at 1538 cm^{-1} was still detected in $V_{0.05}$-MnO_x. In comparison with *in situ* IR spectra of the MoO_3+$Mn_2V_2O_7$ sample (which lacks redox properties at low temperature) (Figure S7), it is concluded that the NH_2 species arose from

the activation of the adsorbed NH_3 on Mn_2O_3. Moreover, despite the high amount of Brønsted acidity in the MoO_3+$Mn_2V_2O_7$ sample, its poor SCR activity may indicate that the Lewis acidity may play a crucial role in the SCR reaction at low temperature (Figure 3 and Figure S7).[24]

4.4 Transfer of reaction intermediates and reaction mechanism

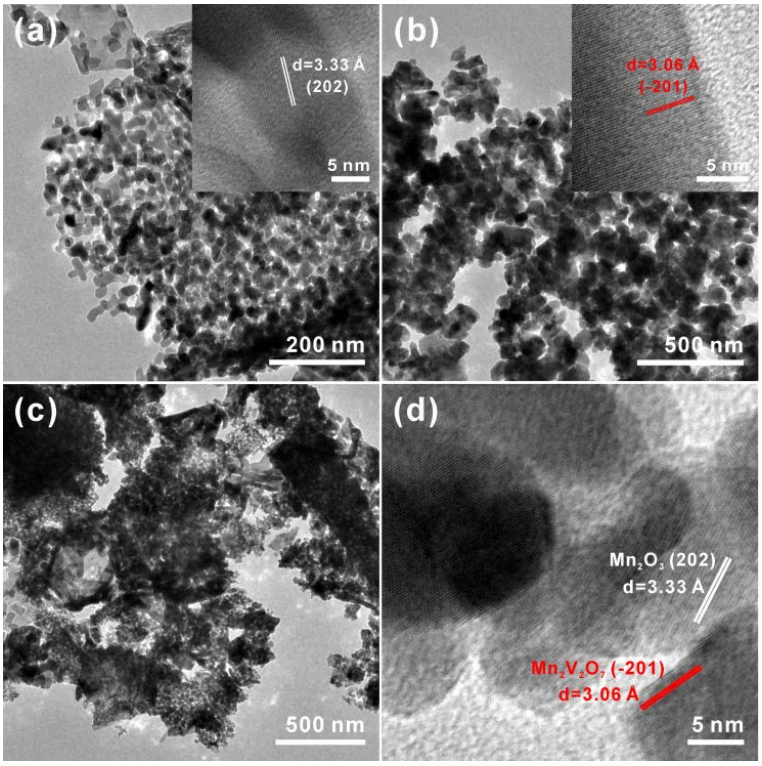

Figure 7. TEM and HRTEM images of (a) Mn_2O_3, (b) $Mn_2V_2O_7$, (c, d) $V_{0.05}$-MnO_x.

TEM characterization reveals that the nanoparticles are aggregated together with ~20 (Figure 7a) and ~80 nm in diameter (Figure 7b) for Mn_2O_3 and $Mn_2V_2O_7$, respectively. The close proximity of Mn_2O_3 and $Mn_2V_2O_7$ particles in V_a-MnO_x is demonstrated in the example of $V_{0.05}$-MnO_x (Figure 7c and d). This again may be seen as evidence that the higher activity of V_a-MnO_x compared with Mn_2O_3 which contributes to the synergism between Mn_2O_3 and $Mn_2V_2O_7$. It is

likely that the NH_2 intermediate from NH_3 partial oxidation on Mn_2O_3 transfers to $Mn_2V_2O_7$ where the further reactions of NH_2 with gaseous NO ultimately produce N_2 rather than N_2O over Mn_2O_3. Following this assumption, it could be the case that $V_{0.05}$-MnO_x, which shows the maximum activity, exhibits the optimal contact between Mn_2O_3 and $Mn_2V_2O_7$, thus facilitating transfer of intermediates. According to the physical dimensions of Mn_2O_3 and $Mn_2V_2O_7$ nanoparticles in V_a-MnO_x, the optimal ratio of Mn_2O_3 and $Mn_2V_2O_7$ is calculated by assuming that the particles are spherical and tangentially contacted (Figure 8). At most, one hundred Mn_2O_3 spherical particles are at a tangent with the surface of one $Mn_2V_2O_7$ particle, while for one Mn_2O_3 spherical particle, only 6.25 $Mn_2V_2O_7$ particles are located at its external surface tangentially. Therefore, the calculated optimal matching value for the molar ratio between Mn_2O_3 and $Mn_2V_2O_7$ is 16, which is very close to those of the calculated molar ratios from theoretical values and quantitative XRD analysis for $V_{0.05}$-MnO_x (Table 1). This confirms that the optimal activity of $V_{0.05}$-MnO_x is a consequence of the optimal contact arising between the two components which facilitate the transfer of the active intermediates. Anyway, the transfer process will be corroborated by the following DFT calculations.

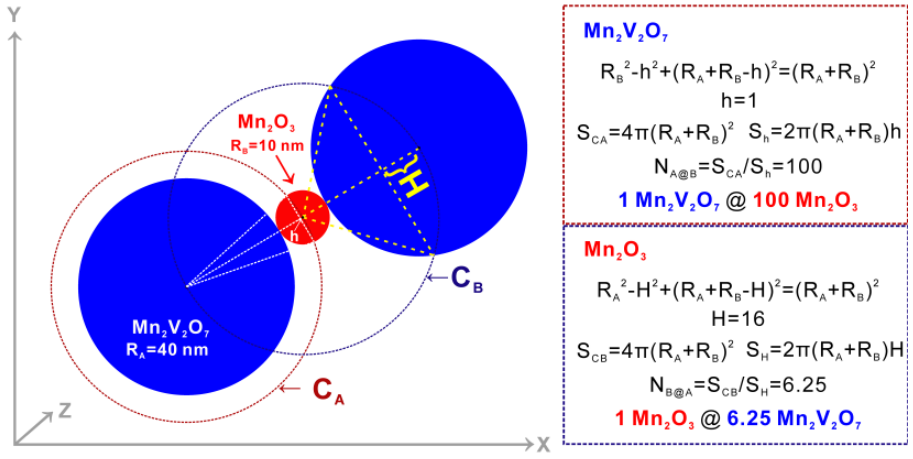

Figure 8. The simulated geometric configuration and calculation formulas for the optimal contact between the two different phases.

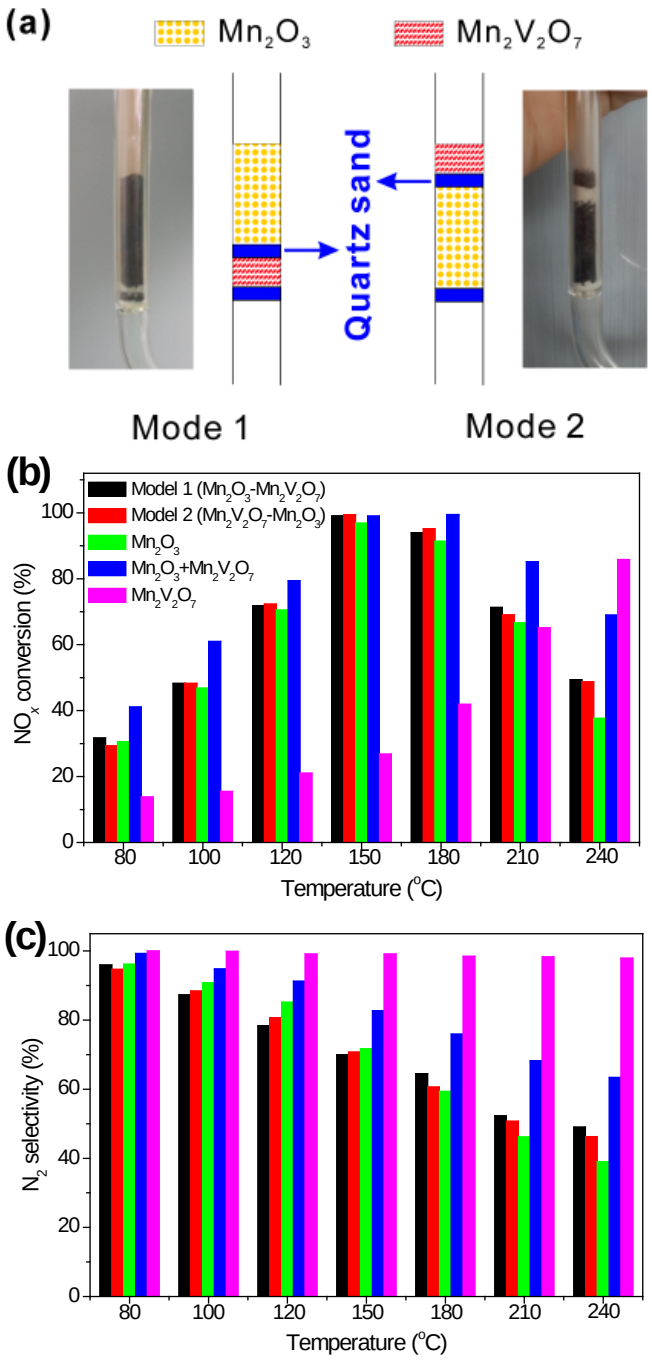

Figure 9. (a) Photographs and schematic graphs of Mode 1 and 2, (b) NO_x conversion and (c) N_2 selectivity of the Mode 1 and 2 samples. Dual-bed configuration with Mn_2O_3 packed above (Mode 1) or below (Mode 2) $Mn_2V_2O_7$ and separated by a layer of quartz sand.

To further demonstrate the transfer of the reactive intermediate, SCR reactions over the catalysts with the two functionalities packed in different modes under the same conditions were performed (Figure 9a). Irrespective of Mode 1 or 2, the negligible improvement in activity was observed compared with Mn_2O_3 (Figure 9b and c) indicating that even though the active intermediates are generated over Mn_2O_3, transfer cannot proceed (Mode 1) due to the long-distance between the two components. In addition, the activity of the Mn_2O_3+$Mn_2V_2O_7$ sample is higher than those of Mode 1 and 2 (Figure 9b and c), confirming that tight contact is indispensable, as in the case of V_a-MnO_x.

Further investigation of the transferred NH_2 from Mn_2O_3 with gaseous NO on $Mn_2V_2O_7$ was conducted using *in situ* IR spectra of the SCR reaction over $V_{0.05}$-MnO_x (Figure 6d). In comparison with Figure 6c, a unique band at ~1325 cm^{-1} which was not found over pure Mn_2O_3 and $Mn_2V_2O_7$ samples could be attributed to N=O stretching vibration. However, in the surface reactions on $V_{0.05}$-MnO_x between not only NO+O_2 and pre-adsorbing NH_3 (Figure S8a) but also NH_3 and pre-adsorbed NO+O_2 (Figure S8b), the ~1325 cm^{-1} band is similarly present, suggesting that it is correlated with both N=O and N-H moieties, most likely due to the NH_2NO species,[78] arising from the combination of the NH_2 species and gaseous NO.[72] This assignment will be shown reasonable by DFT calculations. Thus, the V_a-MnO_x system works as a bifunctional catalyst, in which Mn_2O_3 is responsible for NH_3 activation while $Mn_2V_2O_7$ participates in N_2

production whilst the transfer of the NH_2 intermediate occurs between the two components. Without NH_2 migration from Mn_2O_3 to $Mn_2V_2O_7$, this NH_2 intermediate would be further oxidized to N_2O over the Mn_2O_3. Once NH_2 intermediate is transferred to $Mn_2V_2O_7$, the NH_2NO formed over $Mn_2V_2O_7$ is converted to N_2 rather than N_2O at lower temperature. To verify the above hypothesis, DFT calculations were performed.

4.5 DFT calculations

As displayed in HRTEM images (the insets of Figure 7a and b), the (202) and ($\bar{2}$01) surfaces were exposed for Mn_2O_3 and $Mn_2V_2O_7$, respectively. Consequently, DFT calculation was carried out on Mn_2O_3(202) (Figure S9) and $Mn_2V_2O_7$($\bar{2}$01) (Figure S10). Other considerations for choosing the two facets are provided in Supporting Information.

Firstly, the calculations of NH_3 adsorption were conducted and the corresponding adsorption energies of the most stable configuration (Figure S11) on Mn_2O_3(202) and $Mn_2V_2O_7$($\bar{2}$01) are listed in Table S1. The adsorption energies were calculated on the basis of PBE+*U* and checked by HSE06 calculations. As listed in Table S1, PBE+*U* and HSE06 results are qualitatively consistent. In the case of Mn_2O_3, NH_3 tends to adsorb atop at the Lewis acid sites of Mn^{I}_{4c} (4-fold coordinated Mn cation) rather than at the Brønsted site of HO^{I}_{2c} (two-fold coordinated oxygen anion) over Mn_2O_3(202). Moreover, the adsorption energy of NH_3 is evidently stronger than that of NO over Mn_2O_3(202), suggesting that the Lewis acid site of Mn would be occupied by NH_3 while NO is difficult to adsorb on the surface. In the case of $Mn_2V_2O_7$, NH_3 also preferentially adsorbs at the Lewis acid site of Mn^{I}_{5c} (Mn^{I}_{5c}5-fold coordinated Mn cation) rather than at the Brønsted site of HO_{1c}(one-fold coordinated oxygen anion) over $Mn_2V_2O_7$($\bar{2}$01). Nevertheless, the adsorption strength of NH_3 over $Mn_2V_2O_7$($\bar{2}$01) is weaker than that over Mn_2O_3(202) at

Lewis acid sites while the order of NH_3 binding strength is reversed at Brønsted site due to the existence of one-fold coordinated oxygen at $Mn_2V_2O_7(\bar{2}01)$. These facts imply a stronger Lewis acidity of Mn cations at the $Mn_2O_3(202)$ surface compared with those in the $Mn_2V_2O_7(\bar{2}01)$ surface. In addition, NO barely adsorbs over $Mn_2V_2O_7(\bar{2}01)$, which suggests that the Lewis acid sites would also be occupied by NH_3 on the $Mn_2V_2O_7(\bar{2}01)$ surface. The above results are all in good agreement with the *in situ* IR characterization.

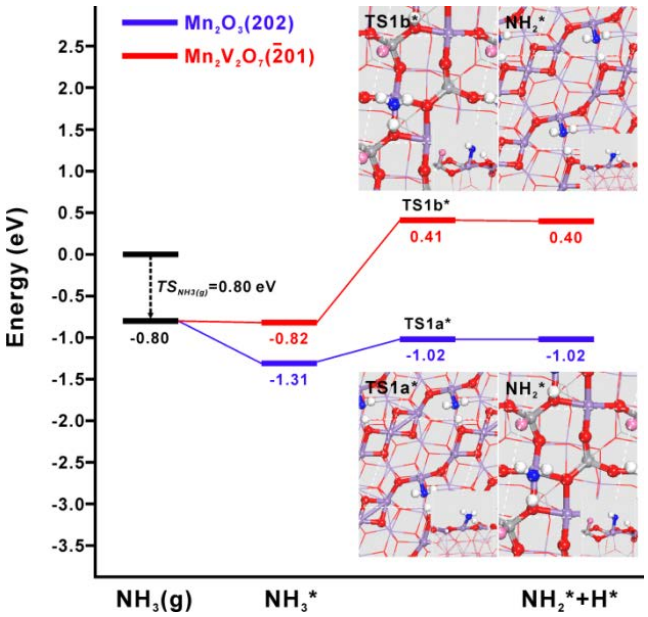

Figure 10. Energy profiles of NH_3 adsorption and its oxidative dehydrogenation over $Mn_2O_3(202)$ and $Mn_2V_2O_7(\bar{2}01)$ considering the large entropy of gaseous NH_3 (T = 400 K, TS = 0.80 eV) and the corresponding transition state structures of TS1a* and TS1b* and final states of adsorbed NH_3^* oxidative dehydrogenation over these two surfaces, respectively.

Since NH_3 exposure prior to NO adsorbs at Lewis acid sites over both $Mn_2O_3(202)$ and $Mn_2V_2O_7(\bar{2}01)$, we further explored NH_3 oxidative dehydrogenation over $Mn_2O_3(202)$ and $Mn_2V_2O_7(\bar{2}01)$ at a reaction temperature of 400 K. As shown in Figure 10, not only is the adsorption strength of NH_3 on $Mn_2O_3(202)$ stronger than on $Mn_2V_2O_7(\bar{2}01)$ but also the NH_3 activation barrier of 0.29 eV on $Mn_2O_3(202)$ is much lower in comparison with 1.23 eV for $Mn_2V_2O_7(\bar{2}01)$, indicating that Mn_2O_3 with excellent oxidation properties can readily activate the adsorbed NH_3 to form $NH_2^*+H^*$ (* denotes the adsorbed species) which is demanding on $Mn_2V_2O_7(\bar{2}01)$.

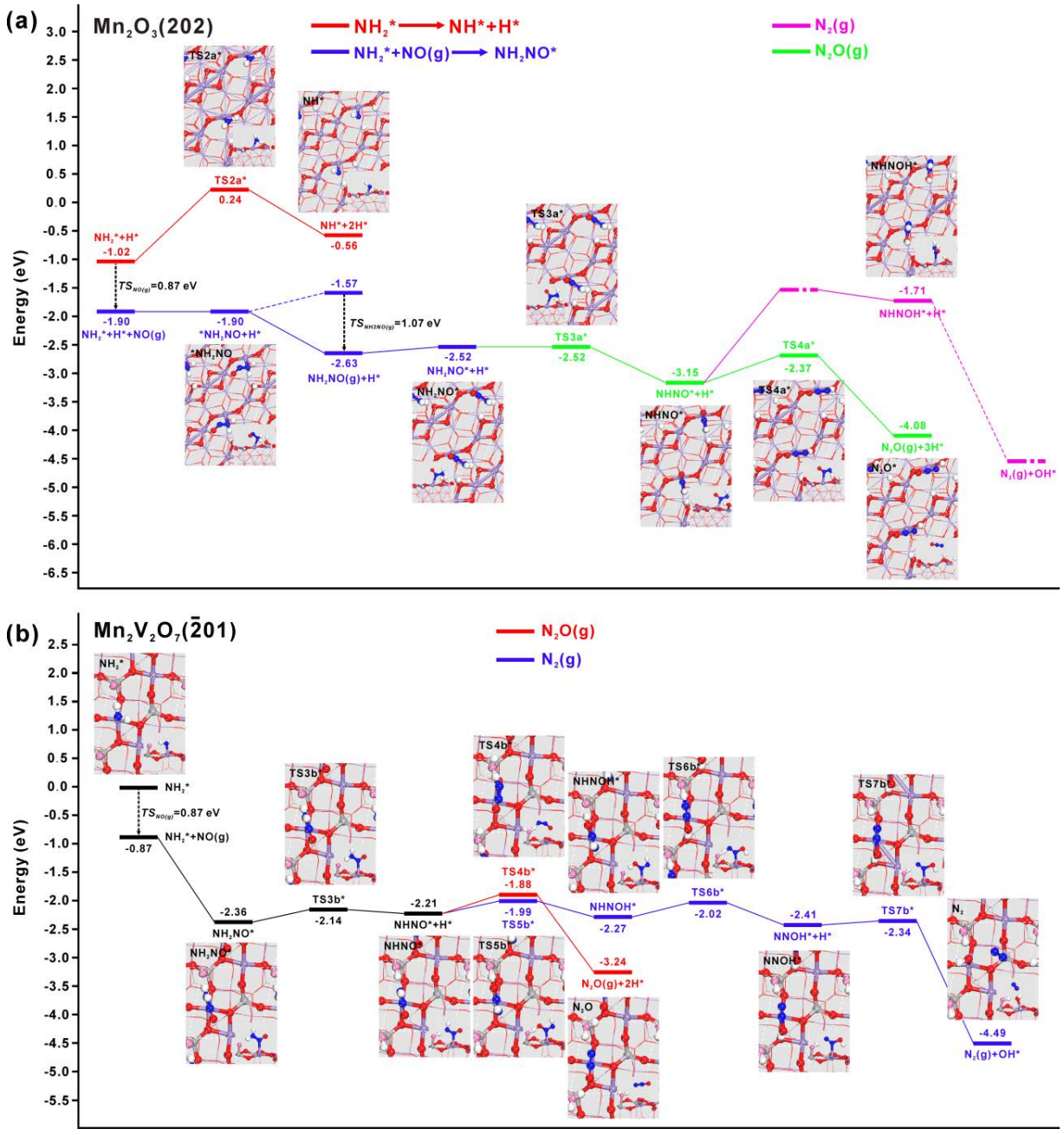

436

437 **Figure 11.** (a) Energy profiles and the corresponding transition states and intermediate states

438 geometry structures of the oxidative dehydrogenation of NH_2* and the formation of N_2O and N_2

439 processes over Mn_2O_3(202) considering the great entropy of gaseous NO and NH_2NO (T = 400

440 K, TS_{NO} = 0.87 eV and TS_{NH_2NO} = 1.07 eV); (b) Energy profiles and the corresponding transition

441 states and intermediate states geometry structures of N_2O and N_2 formation over $Mn_2V_2O_7$(2̄01)

after the migration of NH_2^* from $Mn_2O_3(202)$ to $Mn_2V_2O_7(\bar{2}01)$ considering the great entropy of gaseous NO and NH_2NO (T = 400 K, TS_{NO} = 0.87 eV).

Accordingly, the subsequent reaction channels beginning with NH_2^* including the possible further oxidative dehydrogenation of NH_2^* were investigated over $Mn_2O_3(202)$. As shown in Figure 11a, on the one hand, the energy barrier for NH_2^* oxidative dehydrogenation to NH^* is as high as 1.26 eV, leading to the outcome that the formation of NH^*+2H^* from activated $NH_2^*+H^*$ via this pathway, i.e. the deep oxidative dehydrogenation of NH_3 would not be feasible at low temperature. On the other hand, the formation of $^*NH_2NO$ from NH_2^* and gaseous NO is evidently exothermic, which could compensate for the entropy loss of gaseous NO due to its fixation by the surface. This indicates that NH_2^* tends to associate with gaseous NO to produce $^*NH_2NO$ rather than undergo further dehydrogenation. After the desorption and re-adsorption process, the chemisorption of $^*NH_2NO$ at Mn site will switch from the configuration via the N of NH_2 moiety to the more stable configuration via the N of NO moiety ($^*NH_2NO \rightarrow NH_2NO^*$). The NH_2NO^* formed could then be dehydrogenated to $NHNO^*$ almost without energy barrier which then tends to be further dehydrogenated to form N_2O instead of the more desirable N_2 from the dehydroxylation over $Mn_2O_3(202)$. The formation of N_2 must undergo N-O bond dissociation process. Since the breaking of the single bond of N-O in NHNOH and the formation of monovalent NHN^* and OH^* would be thermodynamically far easier than the breaking of double bond of N=O in NHNO and the formation of bivalent NH_2N^* and O^* with stronger bonding competition at single Mn cation of $Mn_2O_3(202)$, the production of N_2 will pass through $NHNOH^*$ over $Mn_2O_3(202)$. However, since the reaction energy from $NHNO^*$ to $NHNOH^*$ is 1.44 eV, which is even higher than the energy barrier of 0.78 eV for the dehydrogenation of

NHNO* to yield N_2O, N_2O production is more favorable than N_2 over the pure $Mn_2O_3(202)$ surface. This DFT result is consistent with the experimental results of the low N_2 selectivity of Mn_2O_3 in SCR reaction (Figure 3b).

Interestingly, in the presence of the second component of $Mn_2V_2O_7$, despite the tough oxidative dehydrogenation of NH_3 to produce NH_2* over $Mn_2V_2O_7(\bar{2}01)$, once NH_2* is able to migrate to this surface from the $Mn_2O_3(202)$ surface, it is clear from Figure 11b that the energy barriers of the subsequent reaction channels towards the production of N_2O and N_2 are all rather low. Additionally, although the facile energy barrier of oxidative dehydrogenation of NHNO* to yield N_2O over $Mn_2V_2O_7(\bar{2}01)$ (0.33 eV) is evidently lower than that over $Mn_2O_3(202)$ (0.78 eV), the energy barriers in the branch pathway towards the formation of gaseous N_2 starting from NHNO* are all even lower than the energy barrier of N_2O formation over $Mn_2V_2O_7(\bar{2}01)$. This might be attributed to the presence of one-fold coordinated lattice oxygen anion at the surface of $Mn_2V_2O_7(\bar{2}01)$ with stronger Lewis basicity and steric structure advantage which is in favor of the hydrogen transfer between the surface and intermediates via hydrogen bond for the formation of NHNOH* and NNOH*. Thus N_2 production is more favorable than N_2O over $Mn_2V_2O_7(\bar{2}01)$ surface. Furthermore, once NH_2* could readily migrate to $Mn_2V_2O_7$ from Mn_2O_3, the formation of N_2O over the $Mn_2O_3(202)$ surface could be suppressed. This sheds light on the fact that N_2 could be rapidly and selectively produced utilizing V_a-MnO_x catalysts, which also underscores the significance of the existence of Mn_2O_3 which is capable of activating NH_3 to form NH_2* and the intimate contact between Mn_2O_3 and $Mn_2V_2O_7$ on which NH_2* migration depends.

Combining experimental results with DFT calculations, we conclude that the SCR reaction over this bifunctional catalyst mainly follows the pathway as described: adsorbed NH_3 is activated over Mn_2O_3 into a NH_2 intermediate, which then transfers to $Mn_2V_2O_7$ where it reacts

with gaseous NO to form NH_2NO, which will be exclusively decomposed into N_2. The NO_x conversion on Mn_2O_3 into N_2O is thus inhibited.

5. CONCLUSIONS

In summary, we have fabricated the bifunctional V_a-MnO_x catalysts composed of Mn_2O_3 and $Mn_2V_2O_7$, which separate the activation of NH_3 and the production of N_2 via an active intermediate NH_2 transfer. Both NO_x conversion and N_2 selectivity are greatly improved in comparison with Mn_2O_3 at the low temperature due to the synergism between Mn_2O_3 and $Mn_2V_2O_7$ which enhanced Lewis acid density of V_a-MnO_x. The maximum activity for $V_{0.05}$-MnO_x is attributed to the optimal contact between these two components, highlighting the significance of the proximity for transfer of the intermediate. Using a combination of *in situ* IR characterization and DFT calculations, the NH_2 intermediate was found to be formed by NH_3 dehydrogenation over Mn_2O_3, and to subsequently be transferred and reacted with gaseous NO into NH_2NO on $Mn_2V_2O_7$, which exclusively decomposes into N_2. The deep oxidation of adsorbed NH_3 on Mn_2O_3 into N_2O is therefore inhibited.

ASSOCIATED CONTENT

Supporting Information. Additional characterization data (such as XAFS, Raman, XPS, XRD and *in situ* IR) and theoretical calculation results can be found in the Supporting Information.

AUTHOR INFORMATION

Corresponding Author

*chm_zhangzl@ujn.edu.cn

*xmcao@ecust.edu.cn

*j.anderson@abdn.ac.uk

ACKNOWLEDGEMENTS

This work was supported by National Natural Science Foundation of China (No. 21477046, 21333003 and 21673072) and Key Technology R&D Program of Shandong Province (No. 2016ZDJS11A03). The authors also thank the computing time support from Special Program for Applied Research on Super Computation of the NSFC-Guangdong Joint Fund (the second phase) under Grant No.U1501501.

REFERENCES

(1) Centia, G.; Ciambelli, P.; Perathoner, S.; Russo, P. Environmental catalysis trends and outlook, *Catal. Today* **2002**, 75, 3-15.

(2) Liu, C.; Shi, J. W.; Gao, C.; Niu, C. M. Manganese oxide-based catalysts for low-temperature selective catalytic reduction of NO_x with NH_3: A review, *Appl. Catal. A: Gen.* **2016**, 522, 54-69.

(3) Kang, M.; Park, E. D.; Kim, J. M.; Yie, J. E. Manganese oxide catalysts for NO_x reduction with NH_3 at low temperatures, *Appl. Catal. A: Gen.* **2007**, 327, 261-269.

(4) Liu, Y.; Xu, J.; Li, H. R.; Cai, S. X.; Hu, H.; Fang, C.; Shi, L. Y.; Zhang, D. S. Rational design and *in situ*

fabrication of MnO_2@$NiCo_2O_4$ nanowire arrays on Ni foam as high-performance monolith de-NO_x catalysts, *J. Mater. Chem. A* **2015**, 3, 11543-11553.

(5) Qi, G.; Yang, R. T.; Chang, R. MnO_x-CeO_2 mixed oxides prepared by co-precipitation for selective catalytic reduction of NO with NH_3 at low temperatures, *Appl. Catal. B: Environ.* **2004**, 51, 93-106.

(6) Busca, G.; Lietti, L.; Ramis, G.; Berti, F. Chemical and mechanistic aspects of the selective catalytic reduction of NO_x by ammonia over oxide catalysts: A review, *Appl. Catal. B: Environ.***1998**, 18, 1-36.

(7) Xiong, Y.; Tang, C. J.; Yao, X. J.; Zhang, L.; Li, L. L.; Wang, X. B.; Deng, Y.; Gao, F.; Dong, L. Effect of metal ions doping (M=Ti^{4+}, Sn^{4+}) on the catalytic performance of MnO_x/CeO_2 catalyst for low temperature selective catalytic reduction of NO with NH_3, *Appl. Catal. A: Gen.* **2015**, 495, 206-216.

(8) Liu, F. D.; Yu, Y. B.; He, H. Environmentally-benign catalysts for the selective catalytic reduction of NO_x from diesel engines: structure-activity relationship and reaction mechanism aspects, *Chem. Commun.* **2014**, 50, 8445-8463.

(9) Li, J. H.; Chang, H. Z.; Ma, L.; Hao, J. M.; Yang, R. T. Low-temperature selective catalytic reduction of NO_x with NH_3 over metal oxide and zeolite catalysts—A review, *Catal. Today* **2011**, 175, 147-156.

(10) Zhang, S. G.; Zhang, B. L.; Liu, B.; Sun, S. L. A review of Mn-containing oxide catalysts for low temperature selective catalytic reduction of NO_x with NH_3: reduction mechanism and catalyst deactivation, *RSC Adv.* **2017**, 7, 26226-26242.

(11) Tang, X. F.; Li, J. H.; Sun, L.; Hao, J. M. Origination of N_2O from NO reduction by NH_3 over β-MnO_2 and α-Mn_2O_3, *Appl. Catal. B: Environ.* **2010**, 99, 156-162.

(12) Tang, X. F.; Hao, J. M.; Xu, W. G.; Li, J. H. Low temperature selective catalytic reduction of NO_x with NH_3 over amorphous MnO_x catalysts prepared by three methods, *Catal. Commun.* **2007**, 8, 329-334.

(13) Tian, W.; Yang, H. S.; Fan, X. Y.; Zhang, X. B. Catalytic reduction of NO_x with NH_3 over different-shaped MnO_2 at low temperature, *J. Hazard. Mater.* **2011**, 188, 105-109.

(14) Xu, H. M.; Yan, N. Q.; Qu, Z.; Liu, W.; Mei, J.; Huang, W. J.; Zhao, S. J. Gaseous heterogeneous catalytic reactions over Mn-based oxides for environmental applications: A critical review, *Environ. Sci. Technol.* **2017**, 51, 8879-8892.

(15) Long, R. Q.; Yang, R. T.; Chang, R. Low temperature selective catalytic reduction (SCR) of NO with NH_3

over Fe-Mn based catalysts, *Chem. Commun.* **2002**, 452-453.

(16) Qi, G.; Yang, R. T. Performance and kinetics study for low-temperature SCR of NO with NH_3 over MnO_x-CeO_2 catalyst, *J. Catal.* **2003**, 217, 434-441.

(17) Eigenmann, F.; Maciejewski, M.; Baiker, A. Selective reduction of NO by NH_3 over manganese-cerium mixed oxides: Relation between adsorption, redox and catalytic behavior, *Appl. Catal. B: Environ.* **2006**, 62, 311-318.

(18) Casapu, M.; Krocher O.; Elsener, M. Screening of doped MnO_x–CeO_2 catalysts for low-temperature NO-SCR, *Appl. Catal. B: Environ.* **2009**, 88, 413-419.

(19) Wan, Y. P.; Zhao, W. R.; Tang, Y.; Li, L.; Wang, H. J.; Cui, Y. L.; Gu, J. L.; Li, Y. S.; Shi, J. L. Ni-Mn bi-metal oxide catalysts for the low temperature SCR removal of NO with NH_3, *Appl. Catal. B: Environ.* **2014**, 148-149, 114-122.

(20) Lian, Z. H.; Liu, F. D.; He, H.; Shi, X. Y.; Mo, J. S.; Wu, Z. B. Manganese-niobium mixed oxide catalyst for the selective catalytic reduction of NO_x with NH_3 at low temperatures, *Chem. Eng. J.* **2014**, 250, 390-398.

(21) Chen, Z. H.; Yang, Q.; Li, H.; Li, X. H.; Wang, L. F.; Tsang, S. C. Cr-MnO_x mixed-oxide catalysts for selective catalytic reduction of NO_x with NH_3 at low temperature, *J. Catal.* **2010**, 276, 56-65.

(22) Zuo, J. L.; Chen, Z. H.; Wang, F. R.; Yu, Y. H.; Wang, L. F.; Li, X. H. Low-temperature selective catalytic reduction of NO_x with NH_3 over novel Mn−Zr mixed oxide catalysts, *Ind. Eng. Chem. Res.* **2014**, 53, 2647-2655.

(23) Qi, G.; Yang, R. T. Low-temperature selective catalytic reduction of NO with NH_3 over iron and manganese oxides supported on titania, *Appl. Catal. B: Environ.* **2003**, 44, 217-225.

(24) Smirniotis, P. G.; Peña, D. A.; Uphade, B. S. Low-temperature selective catalytic reduction (SCR) of NO with NH_3 by using Mn, Cr, and Cu oxides supported on hombikat TiO_2, *Angew. Chem. Int. Ed.* **2001**, 40, 2479-2482.

(25) Smirniotis, P. G.; Sreekanth, P. M.; Peña, D. A.; Jenkins, R. G. Manganese oxide catalysts supported on TiO_2, Al_2O_3, and SiO_2: A comparison for low-temperature SCR of NO with NH_3, *Ind. Eng. Chem. Res.* **2006**, 45, 6436-6443.

(26) Park, E.; Kim, M.; Jung, H.; Chin, S.; Jurng, J. Effect of sulfur on Mn/Ti catalysts prepared using chemical vapor condensation (CVC) for low-temperature NO reduction, *ACS Catal.* **2013**, 3, 1518-1525.

(27) Huang, J. H.; Tong, Z. Q.; Huang, Y.; Zhang, J. F. Selective catalytic reduction of NO with NH_3 at low temperatures over iron and manganese oxides supported on mesoporous silica, *Appl. Catal. B: Environ.* **2008**, 78, 309-314.

(28) Singoredjo, L.; Korver, R.; Kapteijn, F.; Moulijn, J. Alumina supported manganese oxides for the low-temperature selective catalytic reduction of nitric oxide with ammonia, *Appl. Catal. B: Environ.* **1992**, 1, 297-316.

(29) Kapteijn, F.; Singoredjo, L.; Driel, M.; Andreini, A.; Moulijn, J. A.; Ramis, G.; Busca, G. Alumina-supported manganese oxide catalysts: II. Surface characterization and adsorption of ammonia and nitric oxide, *J. Catal.* **1994**, 150, 106-115.

(30) Qi, G.; Yang, R. T.; Chang, R. Low-temperature SCR of NO with NH_E over USY-supported manganese oxide-based catalysts, *Catal. Lett.* **2003**, 87, 67-71.

(31) Lou, X. R.; Liu, P. F.; Li, J.; Li, Z.; He, K. Effects of calcination temperature on Mn species and catalytic activities of Mn/ZSM-5 catalyst for selective catalytic reduction of NO with ammonia, *Appl. Surf. Sci.* **2014**, 307, 382-387.

(32) Carja, G.; Kameshima, Y.; Okada, K.; Madhusoodana, C. D. Mn–Ce/ZSM5 as a new superior catalyst for NO reduction with NH_3, *Appl. Catal. B: Environ.* **2007**, 73, 60-64.

(33) Marbán, G.; Valdés-Solís, T.; Fuertes, A. B. Mechanism of low-temperature selective catalytic reduction of NO with NH_3 over carbon-supported Mn_3O_4 Role of surface NH_3 species: SCR mechanism, *J. Catal.* **2004**, 226, 138-155.

(34) Wang, L. S.; Huang, B. C.; Su, Y. X.; Zhou, G. Y.; Wang, K. L.; Luo, H. C.; Ye, D. Q. Manganese oxides supported on multi-walled carbon nanotubes for selective catalytic reduction of NO with NH_3: Catalytic activity and characterization, *Chem. Eng. J.* **2012**, 192, 232-241.

(35) Fang, C.; Zhang, D. S.; Cai, S. X.; Zhang, L.; Huang, L.; Li, H. R.; Maitarad, P.; Shi, L. Y.; Gao, R. H.; Zhang, J. P. Low-temperature selective catalytic reduction of NO with NH_3 over nanoflaky MnO_x on carbon nanotubes in situ prepared via a chemical bath deposition route, *Nanoscale*, **2013**, 5, 9199-9207.

(36) Xiao, X.; Sheng, Z. Y.; Yang L.; Dong, F. Low-temperature selective catalytic reduction of NO_x with NH_3 over a manganese and cerium oxide/graphene composite prepared by a hydrothermal method, *Catal. Sci. Technol*. **2016**, 6, 1507-1514.

(37) Zhang, R. D.; Liu, N.; Luo, Z.; Yang, W.; Liang, X.; Xu, R. N.; Chen, B. H.; Duprez, D.; Royer, S. A remarkable catalyst combination to widen the operating temperature window of the selective catalytic reduction of NO by NH_3, *ChemCatChem* **2014**, 6, 2263-2269.

(38) Salazar, M.; Becker, R.; Grünert, W. Hybrid catalysts–an innovative route to improve catalyst performance in the selective catalytic reduction of NO by NH_3, *Appl. Catal. B: Environ.* **2015**, 165, 316-327.

(39) Salazar, M.; Hoffmann, S.; Tkachenko, O. P.; Becker, R.; Grünert, W. Hybrid catalysts for the selective catalytic reduction (SCR) of NO by NH_3. On the role of fast SCR in the reaction network, *Appl. Catal. B: Environ.* **2016**, 182, 213-219.

(40) Krivoruchenko, D. S.; Telegina, N. S.; Bokarev, D. A.; Stakheev, A. Y. Mn–Ce/beta "bifunctional" catalyst for the selective catalytic reduction of nitrogen oxides with ammonia, *Kinet. Catal.* **2015**, 56, 741-746.

(41) Krivoruchenko, D. S.; Kucherov, A. V.; Telegina, N. S.; Bokarev, D. A.; Selvam, P.; Stakheev, A. Y. Development of the bifunctional catalyst Mn-Fe-Beta for selective catalytic reduction of nitrogen oxides, *Russ. Chem. B.* **2014**, 63, 389-395.

(42) Stakheev, A. Y.; Mytareva, A. I.; Bokarev, D. A.; Baeva, G. N.; Krivoruchenko, D. S.; Kustov, A. L.; Grill, M.; Thøgersen, J. R. Combined catalytic systems for enhanced low-temperature NO_x abatement, *Catal. Today* **2015**, 258, 183-189.

(43) Tang, X. L.; Li, Y. Y.; Yi, H. H.; Yu, Q. J.; Gao, F. Y.; Zhang, R. C.; Li, C. L.; Chu, C. An efficient two-step method for NH_3 removal at low temperature using CoO_x-CuO_x/TiO_2 as SCO catalyst followed by $NiMn_2O_4$ as SCR catalyst, *Energ. Fuel.* **2017**, 31, 8580-8593.

(44) Zhu, M. H.; Lai, J. K.; Tumuluri, U.; Wu, Z. L.; Wachs, I. E. Nature of active sites and surface intermediates during SCR of NO with NH_3 by supported V_2O_5-WO_3/TiO_2 catalysts, *J. Am. Chem. Soc.* **2017**, 139, 15624-15627.

(45) Vuong, T. H.; Radnik, J.; Rabeah, J.; Bentrup, U.; Schneider, M.; Atia, H.; Armbruster, U.; Grünert, W.; Brückner, A. Efficient $VO_x/Ce_{1-x}Ti_xO_2$ catalysts for low-temperature NH_3-SCR: Reaction mechanism and active sites assessed by in situ/operando spectroscopy, *ACS Catal.* **2017**, 7, 1693-1705.

(46) Huang, L.; Zhao, X.; Zhang, L.; Shi, L. Y.; Zhang, J. P.; Zhang, D. S. Large-scale growth of hierarchical transition-metal vanadate nanosheets on metal meshes as monolith catalysts for De-NO_x reaction, *Nanoscale* **2015**, 7, 2743-2749.

(47) Liu, F. D.; He, H.; Lian, Z. H.; Shan, W. P.; Xie, L. J.; Asakura, K.; Yang, W. W.; Deng, H. Highly dispersed iron vanadate catalyst supported on TiO_2 for the selective catalytic reduction of NO_x with NH_3, *J. Catal.* **2013**, 307, 340-351.

(48) Casanova, M.; Nodari, L.; Sagar, A.; Schermanz, K.; Trovarelli, A. Preparation, characterization and NH_3-SCR activity of $FeVO_4$ supported on TiO_2-WO_3-SiO_2, *Appl. Catal. B: Environ.* **2015**, 176-177, 699-708.

(49) Zhao, X.; Huang, L.; Li, H.; Hu, H.; Hu, X. N.; Shi, L. Y.; Zhang, D. S. Promotional effects of zirconium doped $CeVO_4$ for the low-temperature selective catalytic reduction of NO_x with NH_3, *Appl. Catal. B: Environ.* **2016**, 183, 269-281.

(50) Marberger, A.; Elsener, M.; Ferri, D.; Sagar, A.; Schermanz, K.; Kröcher, O. Generation of NH_3 selective catalytic reduction active catalysts from decomposition of supported $FeVO_4$, *ACS Catal.* **2015**, 5, 4180-4188.

(51) Wu, G. X.; Li, J.; Fang, Z. T.; Lan, L.; Wang, R.; Gong, M. C.; Chen, Y. Q. $FeVO_4$ nanorods supported TiO_2 as a superior catalyst for NH_3–SCR reaction in a broad temperature range, *Catal. Commun.* **2015**, 64, 75-79.

(52) Casanova, M.; Schermanz, K.; Llorca, J.; Trovarelli, A. Improved high temperature stability of NH_3-SCR catalysts based on rare earth vanadates supported on TiO_2–WO_3–SiO_2, *Catal. Today* **2012**, 184, 227-236.

(53) Salazar, M.; Hoffmann, S.; Tillmann, L.; Singer, V.; Becher, R. Hybrid catalysts for the selective catalytic reduction (SCR) of NO by NH_3: Precipitates and physical mixtures, *Appl. Catal. B: Environ.* **2017**, 218, 793-802.

(54) Chung, F. H. Quantitative interpretation of X-ray diffraction patterns of mixtures. I. Matrix-flushing method for quantitative multicomponent analysis, *J. Appl. Cryst.* **1974**, 7, 519-525.

(55) Newville, M. IFEFFIT: interactive XAFS analysis and FEFF fitting, *J. Synchrotron Radiat.* **2001**, 8, 322-324.

(56) Kresse, G.; Furthmüller, J. Efficient iterative schemes for *ab initio* total-energy calculations using a plane-wave basis set, *Phys. Rev. B* **1996**, 54, 11169-11186.

(57) Kresse, G.; Furthmüller, J. Efficiency of ab-initio total energy calculations for metals and semiconductors using a plane-wave basis set, *Comp. Mater. Sci.* **1996**, 6, 15-50.

(58) Kresse, G.; Joubert, D. From ultrasoft pseudopotentials to the projector augmented-wave method, *Phys. Rev. B* **1999**, 59, 1758-1775.

(59) Perdew, J. P.; Burke, K.; Ernzerhof, M. Generalized gradient approximation made simple, *Phys. Rev. Lett.* **1996**, 77, 3865-3868.

(60) Grant, R. W.; Geller, S.; Cape, J. A.; Espinosa, G. P. Magnetic and crystallographic transitions in the α-Mn_2O_3-Fe_2O_3 system, *Phys. Rev.* **1968**, 175, 686-695.

(61) Wang, L.; Maxisch, T.; Ceder, G. Oxidation energies of transition metal oxides within the GGA+U framework, *Phys. Rev. B* **2006**, 73, 195107.

(62) He, Z. Z.; Ueda, Y. Magnetic properties of $Mn_2V_2O_7$ single crystals, *J. Solid State Chem.* **2008**, 181, 235-238.

(63) Yan, Q. M.; Li, G.; Newhouse, P. F.; Yu, J.; Persson, K. A.; Gregoire, J. M.; Neaton, J. B. $Mn_2V_2O_7$: An earth abundant light absorber for solar water splitting, *Adv. Energy Mater.* **2015**, 1401840.

(64) Michaelides, A.; Hu, P.; Alavi, A. Physical origin of the high reactivity of subsurface hydrogen in catalytic hydrogenation, *J. Chem. Phys.* **1999**, 111, 1343-1345.

(65) Liu, Z. P.; Hu, P. General trends in the barriers of catalytic reactions on transition metal surfaces, *J. Chem. Phys.* **2001**, 115, 4977-4980.

(66) Hu, W. D.; Lan, J. G.; Guo, Y.; Cao, X. M.; Hu, P. Active low-coordination lattice oxygen and cooperation of multiple active sites, *ACS Catal.* **2016**, 6, 5508-5519.

(67) Heyd, J.; Scuseria, G. E. Efficient hybrid density functional calculations in solids: Assessment of the Heyd-Scuseria-Ernzerhof screened Coulomb hybrid functional, *J. Chem. Phys.* **2004**, 121, 1187-1192.

(68) Li, P.; Xin, Y.; Li, Q.; Wang, Z. P.; Zhang, Z. L.; Zheng, L. R. Ce−Ti amorphous oxides for selective

catalytic reduction of NO with NH_3: Confirmation of Ce−O−Ti active sites, *Environ. Sci. Technol.* **2012**, 46, 9600-9605.

(69) Jeong, J.; Aetukuri, N.; Graf, T.; Schladt, T. D.; Samant, M. G.; Parkin, S. S. P. Suppression of metal-insulator transition in VO_2 by electric field-induced oxygen vacancy formation, *Science*, **2013**, 339, 1402-1405.

(70) Silversmit, G.; Depla, D.; Poelman, H.; Marin, G. B.; Gryse, R. D. Determination of the V2p XPS binding energies for different vanadium oxidation states (V^{5+} to V^{0+}), *J. Electron Spectrosc.* **2004**, 135, 167-175.

(71) Topsøe, N. Y. Mechanism of the selective catalytic reduction of nitric oxide by ammonia elucidated by in situ on-line Fourier transform infrared spectroscopy, *Science* **1994**, 265, 1217-1219.

(72) Chen, L.; Li, J. H.; Ge, M. F. DRIFT study on cerium−tungsten/titiania catalyst for selective catalytic reduction of NO_x with NH_3, *Environ. Sci. Technol.* **2010**, 44, 9590-9596.

(73) Centeno, M. A.; Carrizosa, I. Odriozola, J. A. NO–NH_3 coadsorption on vanadia/titania catalysts: determination of the reduction degree of vanadium, *Appl. Catal. B: Environ.* **2001**, 29, 307-314.

(74) Liu, F. D.; He, H.; Zhang, C. B.; Shan, W. P.; Shi, X. Y. Mechanism of the selective catalytic reduction of NO_x with NH_3 over environmental-friendly iron titanate catalyst, *Catal. Today* **2011**, 175, 18-25.

(75) Amores, J. M. G.; Escribano, V. S.; Ramis, G.; Busca, G. An FT-IR study of ammonia adsorption and oxidation over anatase-supported metal oxides, *Appl. Catal. B: Environ.* **1997**, 13, 45-58.

(76) Wu, Z. B.; Jiang, B. Q.; Liu, Y.; Wang, H. Q.; Jin, R. B. DRIFT study of manganese-titania-based catalysts for low-temperature selective catalytic reduction of NO with NH_3, *Environ. Sci. Technol.* **2007**, 41, 5812-5817.

(77) Qi, G.; Yang, R. T. MnO_x-CeO_2 mixed oxides prepared by co-precipitation for selective catalytic reduction of NO with NH_3 at low temperatures, *J. Phys. Chem. B* **2004**, 108, 15738-15747.

(78) Li, Q.; Gu, H. C.; Li, P.; Zhou, Y. H.; Liu, Y.; Qi, Z. N.; Xin, Y.; Zhang, Z. L. In situ IR studies of selective catalytic reduction of NO with NH_3 on Ce-Ti amorphous oxides, *Chinese J. Catal.* **2014**, 35, 1289-1298.

Table of Contents

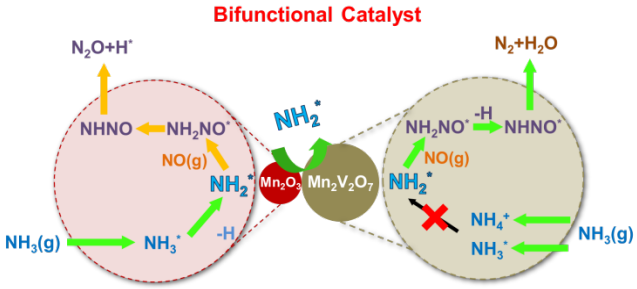
Bifunctional Catalyst
N2O+H*
NHNO
NH2NO*
NO(g)
NH2*
NH3(g)
NH3*
-H
Mn2O3
Mn2V2O7
NH2*
N2+H2O
NH2NO*
-H
NHNO*
NO(g)
NH2*
NH4+
NH3*
NH3(g)

733